

Experimental investigation of the effects of heterogeneity and geostress difference on the 3D growth and distribution of hydrofracturing cracks in unconventional reservoir rocks



Peng Liu ^a, Yang Ju ^{b, c, *}, Pathegama G. Ranjith ^d, Zemin Zheng ^a, Jialiang Chen ^a

^a School of Mechanics and Civil Engineering, China University of Mining & Technology at Beijing, D11 Xueyuan Road, Beijing 100083, China

^b State Key Laboratory of Coal Resources & Safe Mining, China University of Mining & Technology at Beijing, D11 Xueyuan Road, Beijing 100083, China

^c State Key Laboratory for Geomechanics & Deep Underground Engineering, China University of Mining & Technology, No 1 University Avenue, Xuzhou 221116, China

^d Department of Civil Engineering, Monash University, Clayton, Melbourne, Victoria 3800, Australia

ARTICLE INFO

Article history:

Received 25 April 2016

Received in revised form

20 July 2016

Accepted 30 August 2016

Available online 31 August 2016

Keywords:

Hydrofracturing

Unconventional reservoir rock

Heterogeneity

Geostress difference

CT identification

Fractal description

ABSTRACT

Accurate understanding and characterization of the growth and distribution of hydrofracturing cracks is a pivotal issue in enhancing hydraulic fracturing stimulation of unconventional oil and gas reservoirs. In-situ investigations have been conducted to probe hydrofracturing crack growth and distribution patterns underground. Unfortunately, few are available for providing accurate knowledge of the three-dimensional growth and distribution behavior of hydrofracturing cracks in unconventional heterogeneous rock formations. This study reports an investigation that incorporates model materials, triaxial hydrofracturing tests, CT technology, and numerical tools to probe the effects of material heterogeneity and geostress difference on the crack growth and distribution in three dimensions in heterogeneous rocks. The initiation positions and propagation azimuths of cracks influenced by geostress difference and heterogeneous gravels are analyzed by means of fracture mechanics and finite element methods. The CT technique and the fractal theory are used to characterize the 3D growth and distribution patterns of cracks in the media. The results show that material heterogeneity and horizontal geostress difference greatly influence the 3D initiation, growth and distribution of hydrofracturing cracks. The horizontal geostress ratio 1:1.7 appears to be a threshold value lower than which multiple, twist hydrofracturing cracks emerge in heterogeneous reservoir glutenite.

© 2016 Elsevier B.V. All rights reserved.

1. Introduction

Hydrofracturing is one of primary methods that have been widely adopted for stimulation of unconventional natural gas reservoirs. The high-pressure fluid is injected into the reservoirs to fracture rock creating high-conductivity paths for gas migration and thus enhancing gas production. Unconventional natural gas reservoirs usually consist of heterogeneous rocks and suffer complex geostresses. A rising tide of evidence from practical treatment in the field implies that hydrofracturing cracks may initiate and grow in a complicated way that is highly affected by the complexity

of geostresses and the heterogeneity of reservoir formations (Beugelsdijk et al., 2000; Jeffrey et al., 2009; Koceir and Tiab, 2000; Liu et al., 2014b; Mahrer, 1999; Nasehi and Mortazavi, 2013; Sarmadivaleh and Rasouli, 2015; Taleghani, 2010; Teufel and Clark, 1984; Warpinski and Teufel, 1987). Investigations indicate that multiple or twist cracks may emerge as hydrofracturing cracks encounter or intersect with natural geological discontinuities, such as joints, faults, beddings, and inclusions. Understanding the mechanisms and factors that govern the initiation and propagation behavior of hydrofracturing cracks has become a pivotal issue in enhancing hydraulic fracturing stimulation of unconventional gas reservoirs.

To date, in-situ monitoring, laboratory tests and numerical simulations have been conducted to investigate the initiation and growth behavior of hydrofracturing cracks in rock reservoirs. For instance, microseism (MS) technology is often used as an in-situ

* Corresponding author. State Key Laboratory of Coal Resources & Safe Mining, State Key Laboratory for Geomechanics & Deep Underground Engineering, China University of Mining & Technology, D11 Xueyuan Road, Beijing 100083, China.

E-mail address: juy@cumtb.edu.cn (Y. Ju).

measurement to study the crack initiation and propagation in the field (Cipolla et al., 2012b; Gutierrez Murillo et al., 2010; Maxwell and Cipolla, 2011; Warpinski et al., 2009; Waters et al., 2009). When a crack propagates in a 2D plane, microseisms can clearly define the azimuth and geometry of the crack. Nevertheless, accurate crack monitoring depends on interpretation of microseismic data (Cipolla et al., 2012a). Uncertainty of microseismic data will lead to misunderstanding hydrofracturing crack growth and distribution. For example, the uncertainty in arrival times and variations in hodograms could impact the confidence in estimated locations (Castano et al., 2010; Johnston and Shallow, 2011; Maxwell, 2009). Moreover, due to the limitations of azimuthal coverage and the shortage of velocity models, understanding the three-dimensional (3D) crack initiation, propagation and interaction behavior remains a big challenge in MS applications (Gesret et al., 2013; Maxwell et al., 2010). In laboratory tests, acoustic emission (AE), which is known as a typical microseismic method (van der Baan et al., 2013), has been adopted to identify fracture events (Bunger et al., 2015; Chen et al., 2014; Chen et al., 2015; Stanchits et al., 2014; Wasantha et al., 2015). Unfortunately, because of the similar limitations as that of MS in locating fracture events, it is hard for AE methods to appropriately interpret the mechanisms of hydrofracturing crack twist, bifurcation and interaction in three dimensions. Not only this, AE accuracy of locating fractures is highly interfered by the AE sensors that are mounted on the specimens (Nabipour, 2013; Shen et al., 2015). In recent years, researcher adopted advanced techniques, such as X-ray CT (Guo et al., 2014; Hampton et al., 2014; Ju et al., 2015; Zou et al., 2016), nuclear magnetic resonance (NMR) (Adriaensens et al., 2000; Espina et al., 2009; Goma et al., 2014; Grayson et al., 2015), fluorescent (Chen et al., 2015), transparent materials and tracers (Alpern et al., 2012; Thiercelin et al., 1985; Wu et al., 2008a, 2008b), to observe and characterize the invisible cracking behavior inside rocks. Investigations indicate that multiple microcracks occur around the main fracture in granites (Chen et al., 2015; Inui et al., 2014). The hydrofracturing cracks tend to propagate across weaker or smaller density regions subjected to a high geostress difference (Renard et al., 2009). However, it is noteworthy that most of the laboratory tests focus on the hydrofracturing behavior of homogeneous rocks rather than heterogeneous rocks. There is no clear evidence to clarify which factor dominantly governs the hydrofracturing crack initiation and propagation behavior when material heterogeneity and high geostress difference present simultaneously.

In addition to the experimental attempts, analytical and numerical studies of reservoir hydrofracturing have lasted for decades. The early two-dimensional (2D) models, such as PKN models (Nordgren, 1972) and KGD models (Geertsma and De Klerk, 1969), postulate that crack initiates and propagates under the conditions of plane strains, which do not reflect the actual hydraulic fracturing state. To overcome the shortcomings in 2D models, the 3D methods, such as P3D models (Advani and Lee, 1982; Settari and Cleary, 1982), PL3D models, (Vandamme and Curran, 1989), and the models that take into account the propagation of multiple and non-planar cracks (Dong and De Pater, 2001, 2002; Garcia and Teufel, 2005; Hossain and Rahman, 2008; Rungamornrat et al., 2005), have been proposed. Unfortunately, these analytical models have difficulties in explaining the mechanisms of crack twist behavior (Xie et al., 2016) and propagation mechanisms and fluid-solid coupling effects (Liu et al., 2003, 2014a; Nassir et al., 2010; Wang et al., 2012; Zhang et al., 2011, 2014). Recently, diverse numerical methods have been developed to analyze crack initiation and propagation behavior, to mention a few, such as distinct element methods (DEM) (Al-Busaidi et al., 2005; Detournay et al., 2013; Hiyama et al., 2013; Potyondy and Cundall, 2004; Shimizu et al., 2011, 2014), unconventional fracture models (UFM)

(Kresse et al., 2011, 2013), BEM (Zhang et al., 2007), XFEM (Wang et al., 2015), DDM (Gu et al., 2008), and rock failure process analysis (RFPA) (Li et al., 2013; Tang et al., 2002; Wang et al., 2013; Yang et al., 2004). It should be noted that in most cases the heterogeneity of rock formation used to be ignored to simplify numerical computation. However, investigations have proved that material heterogeneity apparently affects the stress intensity factor that is used for judging crack initiation and propagation in the material (Gu and Siebrits, 2008; Simonson et al., 1978; Teufel and Clark, 1984; Zhao and Chen, 2010). One approach to handling this is to postulate that rock heterogeneity is characterized by Weibull's distribution law (Li et al., 2013; Zhong et al., 2014). Nonetheless, the effects of interfaces between inclusions and matrices of rock have not been taken into account (Li et al., 2015).

The purpose of this study is to experimentally probe the mechanisms that essentially govern the 3D hydrofracturing crack initiation, growth and distribution in heterogeneous rock. The effects of material heterogeneity and in-situ geostress difference on the crack growth and distribution patterns are investigated through a series of triaxial hydrofracturing tests and CT imaging of rock samples. The modeling materials and relevant techniques are employed to produce the heterogeneous rock specimens. The initiation positions and propagation azimuths of cracks influenced by geostress difference and heterogeneous gravels are analyzed by means of fracture mechanics and finite element methods. The fractal theory is adopted to characterize the 3D morphology of hydrofracturing cracks.

2. Materials and methods

2.1. Materials and specimen preparation

To study the heterogeneity effect of unconventional reservoir rock on its 3D hydrofracturing behavior, the natural glutenite cores that contain randomly distributed gravels were drilled from the unconventional reservoir at depths of 4000 m at the Shengli SINOPEC oil field in the east of China. The detailed information of natural glutenite, including composition, gravel distribution, mechanical properties, was acquired through X-ray diffraction (XRD), X-ray microfocus computed tomography (μ CT), and mechanical testing methods (Ju et al., 2016; Liu et al., 2016), based on which a few artificial cubic cement samples were fabricated to replace the natural glutenite samples for triaxial hydrofracturing tests. Two reasons force us to adopt artificial specimens: the first is that there are insufficient natural glutenite cores for triaxial hydrofracturing tests because of too much drilling expenses, and the second one is that the size of a glutenite core is relatively smaller than the expected size of a hydrofracturing specimen to diminish the size effect on 3D crack propagation.

In order to make the properties of artificial glutenites as close to those of real glutenites as possible, several strategies were adopted in this research. We first measured the mechanical properties of natural glutenite samples, including the uniaxial compressive strength, Young's modulus, Poisson's ratio, and permeability, as listed in Table 1. Additionally, a microfocus X-ray CT system with a spatial resolution up to 4 μ m was employed to identify the heterogeneous composition of natural glutenite. Fig. 1 illustrates the CT testing device and the CT image of a 2D representative cross-section of the glutenite unveiling the irregular geometry of embedded gravels. More details about the tests refer to the references (Ju et al., 2016; Liu et al., 2016).

Secondly, using the test data, we postulated that the heterogeneous glutenite rock is composed of isotropic matrix and randomly distributed irregular gravels. To distinguish the gravels from the matrix, the mineral composition of matrix and gravels were probed

Table 1
Mechanical properties of natural glutenite.

Sample	Uniaxial compressive strength (MPa)	Elasticity modulus (GPa)	Poisson ratio	Porosity (%)	Permeability ($10^{-3}\mu\text{m}^2$)
Glutenite	116	22.97	0.14	7	0.203

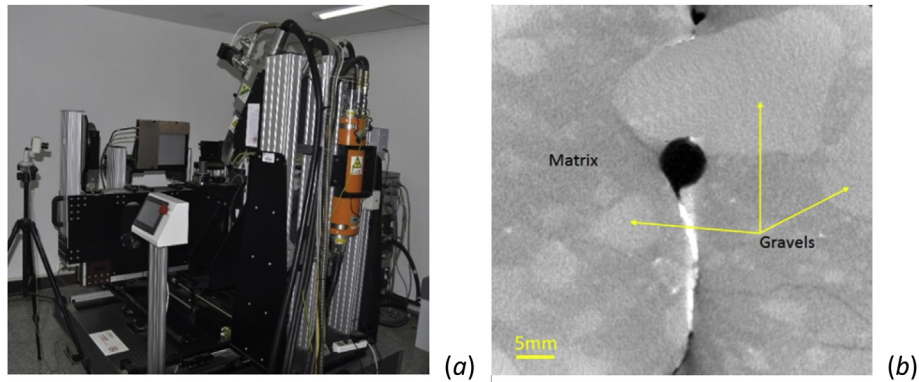


Fig. 1. The microfocus CT system used in the tests (a) and the 2D CT image of the representative cross section of the glutenite core showing its heterogeneous composition and structures (b).

using XRD technology. Table 2 outlines the mineral composition and indicates that dolomite predominates in the mineral composition of gravels. Accordingly, the aedelforsite was chosen as the substitute material due to that its properties such as density and stiffness are similar to those of dolomite. To have an accurate measure of the proportion of gravels to matrices for the artificial models as compared to that of original glutenites, we implemented computed tomography and binary image processing to identify and extract gravels from the matrix of the glutenite sample. Counting the numbers of white and black voxels that comprise gravels and the matrix of a volume sample yields the volume ratio of gravels to matrices, the information of which was then adopted to fabricate an artificial specimen. Fig. 2 plots the grading of gravels that was acquired from the CT images. This process ensures that an artificial specimen has an identical proportion of gravels to matrices comparing with real glutenite samples. The volume proportion of gravels to the volume of an entire specimen is 28.5%. Furthermore, we mixed natural aedelforsites and cement to produce the artificial glutenite specimens that are characterized with the same composition and spacial distribution of gravels as compared to those of prototype glutenite specimens. Table 3 gives the composition and mixture ratio of the raw materials that were used for producing glutenite models. Furthermore, the specimens were cured under a high temperature up to 90 °C for 72 h to ensure that the uniaxial compressive strength that was used as a target index can be achieved. The preparation procedure of artificial specimens actually originates from the method that was proposed to produce reactive powder concrete (RPC) (Richard and Cheyrezy, 1994, 1995; Ju et al., 2007, 2010). According to the previous work, curing the artificial specimens at this temperature can optimize the hydration reaction between the cementitious constituents and then obtain a higher

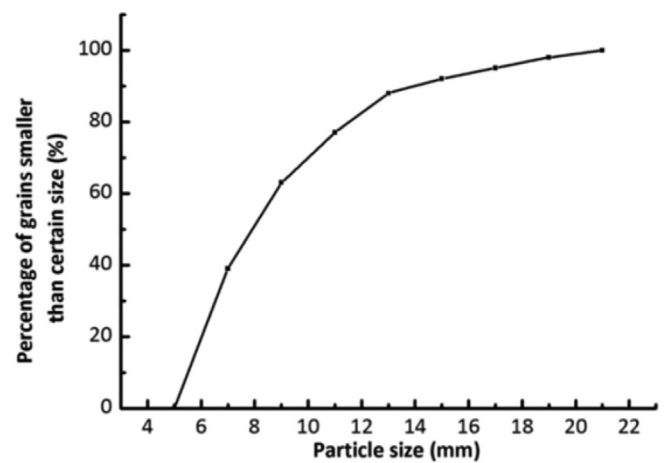


Fig. 2. Size distribution curve of gravels in glutenite.

strength of the material as compared to curing at any other temperature levels. This technique was employed to make the mechanical properties of an artificial specimen as close to those of real glutenite cores as possible.

Thirdly, we conducted laboratory tests to verify whether the artificial samples perform the same mechanical properties as original ones. Table 4 lists the measured mechanical properties of the artificial specimens for comparison. Comparison between the results of artificial samples (Table 4) and original one (Table 1) shows that the uniaxial compressive strength and Young's modulus are fairly close each other, but the Poisson's ratio exhibits a certain

Table 2
Mineral composition of natural glutenite.

Glutenite	Mineral composition (%)					Clay mineral
	Quartz	Potassium feldspar	Anorthose	Calcite	Dolomite	
Matrices	30.2	15.1	37.3	4.5	/	12.9
Gravels	4.0	0.8	5.4	0.5	84.5	4.8

Table 3
Cement mix proportions.

Size (mm)	Water cement ratio	Sand (g)	Cement (g)	Water (g)	Water reducer (g)
100 × 100 × 100	0.2	111	991.3	198.2	24.7

Table 4
Mechanical parameters of artificial specimens.

Specimens	Uniaxial compressive strength (MPa)	Elasticity modulus (GPa)	Poisson ratio	Tensile strength (MPa)
Overall	94.7	30.82	0.26	5.7
Matrices	67.3	22.5	0.3	5.7

degree of deviation. However, considering the purpose of this study, we used identical cement materials and mix proportion to fabricate heterogeneous and homogeneous models for testing the effects of heterogeneity on the hydrofracturing behavior of heterogeneous rock. We mainly focused our attention on the characteristics of randomly distributed gravels and the comparability of the mechanical properties between homogenous and heterogeneous models. The inconsistency of Poisson's ratio between prototypes and models was not emphasized in the analysis.

Note that the present direct tensile strength is determined according the measured relationship between a split tensile strength and a direct tensile strength of the material (Ju et al., 2007, 2010; 2011, 2015).

The cubic specimens with a side length of 100 mm were casted for triaxial hydrofracturing tests. A vertical hole with a diameter 10 mm was dug at the center of a specimen, and a steel borehole packer was inserted into the hole to fit the connector on the top of the specimen. The packer connector is connected to the high-pressure injecting tube by a threaded. The length of the upper portion of the borehole packer is 25 mm, and it was fastened to the borehole wall using anchor glue to seal the open hole under the borehole packer. Fig. 3 diagrams the details of the prepared hydrofracturing specimen.

2.2. Hydrofracturing experiments

Fig. 4 illustrates the triaxial hydrofracturing device used for

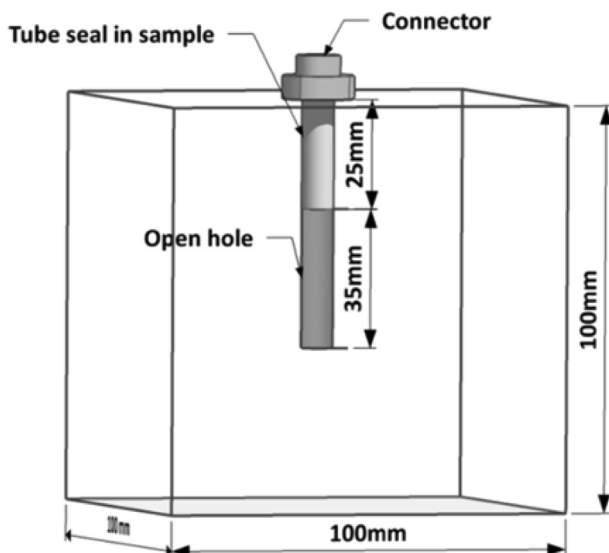


Fig. 3. A schematic of the sample for triaxial hydraulic fracturing tests.

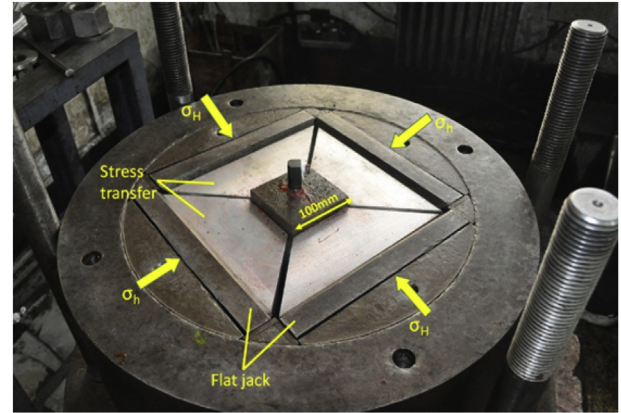


Fig. 4. Photograph of the triaxial hydrofracturing testing device.

fracturing rocks (Zhang and Fan, 2014). To probe the effects of geostress difference in various directions on hydraulic fracturing, the various stresses were applied to the sample along the principal stress directions, i.e. the maximum horizontal geostress (σ_H), the minimum horizontal geostress (σ_h), and the vertical stress (σ_z). Five groups of horizontal geostresses were employed in the experiment with a horizontal geostress ratio within the range from 1:1 to 1:1.9 representing the actual range of horizontal geostress difference in most unconventional reservoir formations, according to some in situ testing data of geostress distributed within natural resource reservoirs in China (Zhang et al., 2010; Zhao et al., 2007). The fracturing fluid comprising a mixture of water and guar gum with a viscosity of 0.326 ml/s was adopted in the test to simulate realistic hydrofracturing fluid and conditions that are widely used in reservoir stimulation practice. To exclude the effects of the other hydrofracturing factors, the water injection rate was kept constant under various horizontal geostress ratios. Table 5 specifies the parameters of stresses and fracturing fluid that were used in the experiment.

3. Experimental results and discussion

3.1. Experimental observation of fracture patterns

To alleviate the effects of specimen sizes on hydrofracturing crack growth, we adopted the cubic specimens with a side length of 100 mm, which requires a high-voltage X-ray beam to penetrate the entire specimen for acquiring clear images of fractures. A 410 V-voltage X-ray CT was adopted to image the hydrofracturing cracks in the specimens. The multi-thresholding segmentation method (Kaestner et al., 2008; Ju et al., 2014) was used to enhance the CT images and identify the fractures. Using the proposed

Table 5
Experimental conditions for hydraulic fracturing tests.

Samples	Principal stresses			Fractural fluid	
	σ_h (MPa)	σ_H (MPa)	σ_z (MPa)	Viscosity (mPa s)	Injection rate (mL s ⁻¹)
1	10	10	20	67	0.326
2	10	13	20	67	0.326
3	10	15	20	67	0.326
4	10	17	20	67	0.326
5	10	19	20	67	0.326

segmentation method and the self-developed computer program (Ju et al., 2013, 2014) the original CT images were digitalized into the images that only comprise the pixels of matrix, gravels and fractures. The 3D morphology of cracks was rendered by means of the VG[®] software (http://www.volume_graphics.com/en/products/vgstudio_max) based on a set of processed 2D images, in which the pixel size was 0.144 mm and the interval between the slices was also 0.144 mm. The 3D reconstructed model of hydrofracturing cracks allows us to quantitatively characterize the 3D morphology of the cracks. Fig. 5 illustrates from left to right the top-view photographs of the fractured specimens, the injection pressure curves and the rendered 3D fractured rock, respectively, displaying the hydrofracturing cracks over the entire graveled specimens. For comparison purposes, the hydrofracturing results of homogeneous samples were presented in Fig. 6. The identical hydrofracturing procedure was applied to the homogenous samples. Confined to the length of the article, more details about testing homogeneous specimens can refer to the literature (Ju et al., 2016; Liu et al., 2016). Results indicate that multiple, twist cracks appeared as the horizontal geostress ratio was lower than 1.7. In such circumstances, the hydrofracturing cracks did not initiate along the direction of maximum horizontal stress as assumed in the conventional theory. Instead, the cracks emerged at various positions near the vertical well, propagated along different directions, and formed a complex fracture network after the cracks experienced arrest, deflection and bifurcation processes. It is evident that this complex crack initiation and growth performance is attributed to the existence of rough gravels when compared with the fracturing behavior of homogeneous samples (Ju et al., 2016). Similar scenarios can also be found in a few SEM and microseismic studies of fracturing performance of sandstones (Chitralla et al., 2013; Warpinski et al., 2010). Nevertheless, it was observed that once the horizontal geostress ratio achieved 1.7 a primary crack emerged and propagated along the direction of the maximum horizontal stress. A secondary crack emerged on one side of the primary crack when the hydrofracturing came to the end splitting the specimen into two parts. This phenomena did not appear in the scenario of a geostress ratio lower than 1.7. Similar phenomena were found in our previous studies (Ju et al., 2016; Liu et al., 2016). Thus, on basis of our experimental observation and the CT images of fractures in rock specimens, the ratio 1:1.7 appears to be a threshold value of stress ratio lower than which multiple, twist hydrofracturing cracks emerge in heterogeneous glutenite specimens. The distinct cracking patterns due to the various applied geostress ratios embody the influence of geostress difference on the hydrofracturing behavior of reservoir media.

3.2. Analysis of the mechanisms for hydrofracturing crack initiation and propagation

To interpret the effects of geostress difference on the initiation and propagation behavior of hydrofracturing cracks, a 2D plane strain model is adopted to analyze the stress distribution around

the wellbore.

Fig. 7 diagrams an arbitrarily selected 2D cross section normal to the wellbore axis, showing the local coordinates and the surrounding stresses at the crack tip and the global coordinates around the wellbore. According to the plane strain theory (Fjær et al., 2008), the circumferential stress at an arbitrary point away from the wellbore can be expressed as

$$\sigma_{\beta} = \frac{\sigma_H + \sigma_h}{2} \left(1 + \frac{R_W^2}{r^2} \right) - \frac{\sigma_H - \sigma_h}{2} \left(1 + 3 \frac{R_W^4}{r^4} \right) \cos 2\beta - P_W \frac{R_W^2}{r^2} \quad (1)$$

where σ_H and σ_h refer to the maximum and the minimum horizontal principal stresses, β is the fracture initiation angle, i.e. the azimuth of initial fracture with respect to the direction of the maximum horizontal stress, R_W is the radius of the wellbore, and r is the distance from the initial fracture point to the center of the wellbore (see Fig. 7a). The maximum circumferential stress theory assumes that crack initiates at the point where the circumferential stress reaches its maximum value (Sih and Madenci, 1983; Zhou et al., 2016). It means that $\frac{\partial \sigma_{\beta}}{\partial \beta} = 0$ if the crack initiates. Substituting Eq. (1) yields

$$(\sigma_H - \sigma_h) \sin 2\beta = 0 \quad (2)$$

When $\sigma_H = \sigma_h$, i.e. there is no difference between the horizontal principal stresses, the fracture initiation angle can be an arbitrary value to satisfy Eq. (2). It means that the crack initiates from any point in the vicinity of the wellbore. Considering the actual strength difference of the glutenite at various locations, it is straightforward to understand that multiple cracks could emerge at different positions near the wellbore as long as the maximum circumferential stresses exceed the ultimate tensile strengths of the points of interest. This explains the observed multiple fractures in the glutenite specimen when the horizontal stress ratio is 1:1. In contrast, if $\sigma_H \neq \sigma_h$, the initiation fracture angle complies $\sin 2\beta = 0$, i.e. $\beta = 0^\circ$ or $\beta = 180^\circ$, which implies that the double-wing crack emerges along the maximum horizontal stress direction. This is in line with the observed fracture pattern that a double-wing crack predominately emerges along the maximum horizontal stress direction when the geostress ratio is equal to 1:1.9. In fact, due to existence of heterogeneity of glutenite, the fracture initiation azimuth does not only depend on stress difference but also depend on material heterogeneity. The heterogeneity leads to the non-uniform distribution of the material strengths, and accordingly affects the fracture initiation position and azimuth. The fracture initiation angle β falls within the range between 0° and 180° . This has been verified by the measured fracture patterns of the glutenite under the horizontal geostress ratios of 1:1.3, 1:1.5 and 1:1.7.

Moreover, the maximum circumferential stress theory can also be applied to determining the propagation azimuth along which the initial crack propagates. To achieve the goal, the finite element analysis tool ANSYS[®] solver is used to numerically determine the circumferential stress around the tip of the initial crack. As an

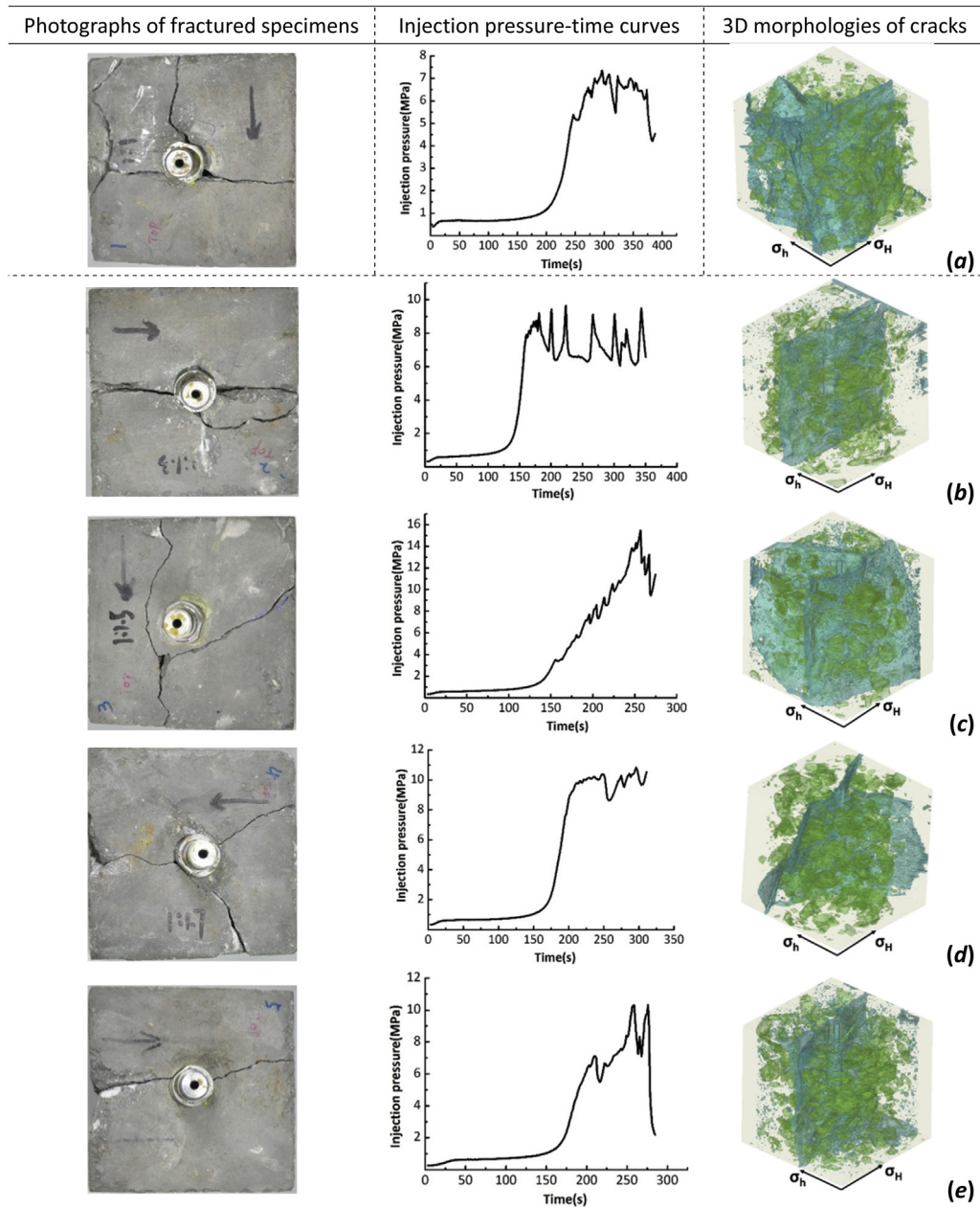


Fig. 5. 3D morphologies of the hydrofracturing cracks of heterogeneous samples. The rows (a) to (e) refer to the results of various geostress with a ratio of 1:1.0, 1:1.3, 1:1.5, 1:1.7, and 1:1.9, respectively. In the 3D reconstructed models, the matrices are transparent, the green parts represent the randomly distributed gravels and the cyan parts refer to the hydrofracturing cracks.

example, Fig. 8 shows the 2D numerical models of the glutenite specimens subjected to the horizontal geostress ratios 1:1.5 and 1:1.7, respectively. To understand the effects of gravels on crack propagation after initiation, the models involve the initial crack

with a certain length. The model was established in ANSYS software using a 2D sectional slice arbitrarily cut out of the 3D fractured model (see Fig. 5). The crack displayed in the model was truncated from the entire propagated crack shown in Fig. 5, keeping the same

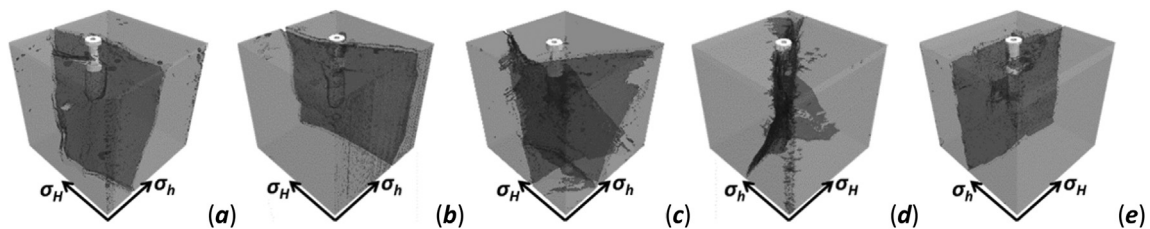


Fig. 6. 3D morphologies of the hydrofracturing cracks of homogeneous samples. The images (a) to (e) refer to the results of various geostress with a ratio of 1:1.0, 1:1.3, 1:1.5, 1:1.7, and 1:1.9, respectively. In the 3D reconstructed models, the matrices are transparent and the black parts refer to the hydrofracturing cracks.

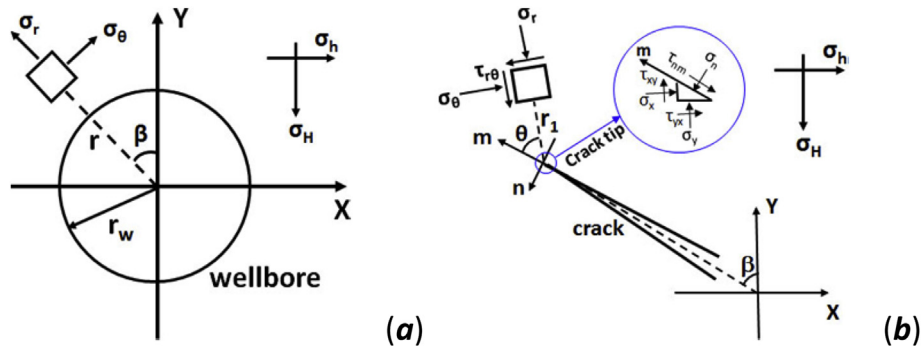


Fig. 7. The schematic diagram of the coordinate system and the stress state around the wellbore (a) and the tip of the initial crack (b).

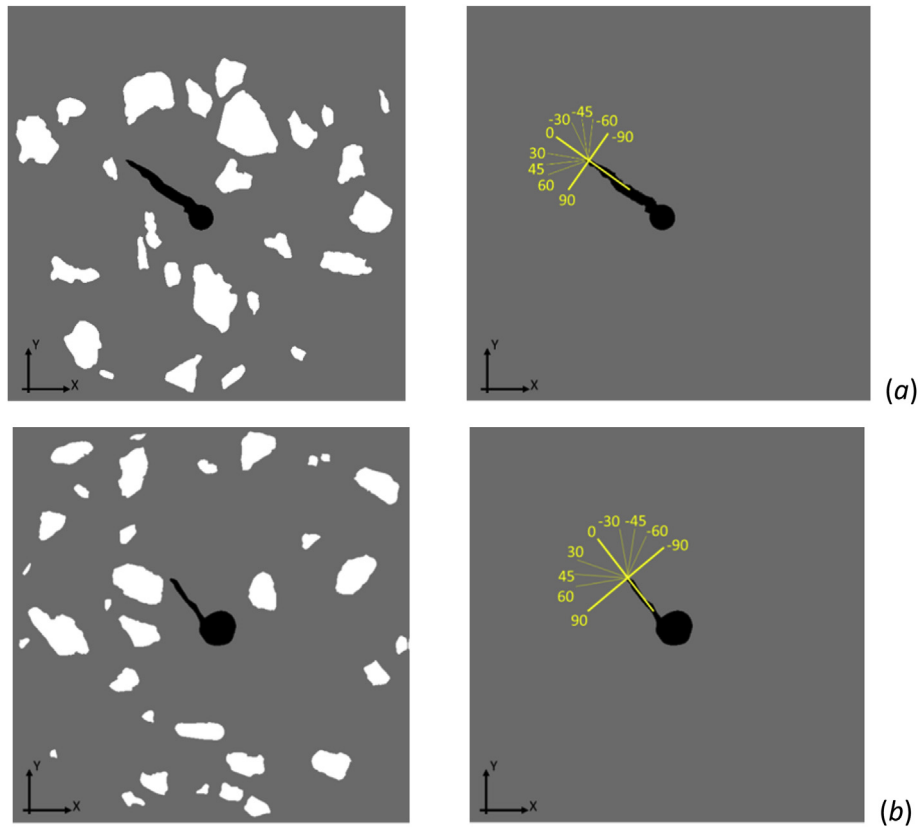


Fig. 8. Numerical models for calculation of the stress distribution around the wellbore: (a) heterogeneous model (left) and homogeneous model (right) subjected to the geostress ratio 1:1.5, (b) heterogeneous model (left) and homogeneous model (right) subjected to the geostress ratio 1:1.7. The grey parts represent homogeneous matrix, the white parts refer to gravels and the dark parts refer to the hydrofracturing crack and the wellbore. The yellow local coordinates at the initial crack tip define the calculation azimuths of crack propagation. (For interpretation of the references to colour in this figure legend, the reader is referred to the web version of this article.)

gravel distribution pattern as that of the specimen before fracturing. In the calculation, water pressure was uniformly applied along the wellbore and the crack surfaces. The horizontal stresses σ_H and σ_h were uniformly applied on the boundary of the model in accordance with the experimental conditions. In order to understand the effect of gravels on stress distribution, the homogeneous rock model with the identical initial crack (see Fig. 8b) was set up for comparing with the heterogeneous glutenite model. The models were meshed in MIMICS® (http://biomedical_materialise.com/mimics) before imported into ANSYS solver for stress calculation. The material properties used in the numerical model were determined according to the experimental results of the artificial glutenite specimens. The Young's modulus and Poisson's ratio of the matrix are considered to be the same as homogeneous samples and

listed in Table 4. The Young's modulus and Poisson's ratio of the gravels was set to be 100 GPa and 0.15 according to the existing results (Peng and Zhang, 2007).

According to the principles of the mixed model of I-II crack propagation (Zhou et al., 2016), the circumferential stress at the tip of initial crack in the coordinate system shown in Fig. 7b, can be expressed as

$$\left. \begin{aligned} \sigma_\theta &= \frac{1}{2\sqrt{2\pi r_1}} \cos \frac{\theta}{2} [K_I (1 + \cos \theta) - 3K_{II} \sin \theta] \\ \tau_{r\theta} &= \frac{1}{2\sqrt{2\pi r_1}} \cos \frac{\theta}{2} [K_I \sin \theta + K_{II} (3 \cos \theta - 1)] \end{aligned} \right\} \quad (3)$$

where θ refers to the propagation azimuth of the initial crack that launches from the tip of the crack (see Fig. 7b), r_1 means the distance between the tip of the initial crack and an arbitrary point in the vicinity of the initial crack, K_I and K_{II} are the stress intensity factors of tensile and shear failure, respectively. The intensity factors K_I and K_{II} can be obtained from Eq. (3) when $\theta = 0$, $r \rightarrow 0$, i.e. $K_I = \lim_{r \rightarrow 0} \sqrt{2\pi r_1} \sigma_\theta(r, 0)$, $K_{II} = \lim_{r \rightarrow 0} \sqrt{2\pi r_1} \tau_{r\theta}(r, 0)$. In this case, $\sigma_\theta(r, 0)$ and $\tau_{r\theta}(r, 0)$ refer to the normal stress σ_n and the shear stress τ_{nm} in m-n coordinate system at the crack tip. Thus, it yields

$$\sigma_\theta = -\frac{1}{2} \cos \frac{\theta}{2} [\sigma_n (1 + \cos \theta) - 3\tau_{nm} \sin \theta] \quad (4)$$

Meanwhile, the stresses σ_n and τ_{nm} can be repressed in the following equations with regard to the global X-Y coordinates (Fjær et al., 2008) shown in Fig. 7b

$$\left. \begin{aligned} \sigma_n &= \frac{1}{2}(\sigma_x + \sigma_y) + \frac{1}{2}(\sigma_x - \sigma_y)\cos 2\beta + \tau_{xy} \sin 2\beta \\ \tau_{nm} &= \frac{1}{2}(\sigma_y - \sigma_x)\sin 2\beta + \tau_{xy} \cos 2\beta \end{aligned} \right\} \quad (5)$$

where σ_x refers to the X-component stress, σ_y means the Y-component stress, and τ_{xy} is the shear stress component in X-Y plane. Figs. 9 and 10 present the calculation results of the stress components σ_x , σ_y and τ_{xy} of both heterogeneous and homogeneous rock models subjected to geostress ratios 1:1.5 and 1:1.7.

According to the maximum circumference theory the crack propagation is governed by the maximum circumference stress. To analyze track the propagation direction of the initial crack, 9 consecutive azimuths (see Fig. 8) were designed to determine and compare their circumferential stresses using Eq. (4). In the calculation, the initial fracture angles β were set to be 45° and 30° for the cases of geostress ratios of 1:1.5 and 1:1.7, respectively. Fig. 11 plots the calculation results.

The calculation indicates that the maximum circumferential stresses of the heterogeneous specimen under different geostress ratios take place along the direction $\theta = -30^\circ$, which means that the crack deflects to the right from its initial azimuth in an angle of

30° (see Fig. 8b). This is consistent with the experimental observation of crack propagation in the heterogeneous media under the same geostress conditions (see Fig. 12). More than that, the comparison in Fig. 11 shows that, for the majority of propagation azimuths (θ), the maximum circumferential stress $\sigma_{\theta, \max}$ at the point of interest of the heterogeneous specimen appears larger than that of the homogeneous specimen. The higher the geostress difference is, the larger the gap between the circumferential stresses appears. In the other words, when increasing the horizontal geostress difference, e.g. the geostress ratio reaches 1:1.7, the circumferential stress that induces crack propagation of heterogeneous media approaches to that of homogeneous media.

Additionally, the numerical analysis indicates that the stress distribution in the vicinity of an initial crack tip is non-uniform even for the homogeneous specimen. Basically, the non-uniform stress distribution is attributed to the coupled effects of geostress difference and material heterogeneity. Our results show that when the geostress difference rises, the degree of non-uniform distribution of interior stresses increases for both heterogeneous and homogeneous media. High-level stress concentrates more in the neighborhood of the initial crack tip other than the distributed gravels. It implies that when applied geostress difference is high, geostress difference governs the non-uniform distribution of interior stresses and then the propagation of initial cracks more than material heterogeneity. The ratio 1:1.7 seems to be the threshold stress ratio below which material heterogeneity plays the dominant role in governing the initial crack propagation rather than geostress difference. This has been verified by our CT observation of the crack growth and propagation in both heterogeneous and homogeneous specimens.

4. Fractal description of 3D hydrofracturing crack network

4.1. Fractal characteristics of 3D hydrofracturing crack networks

The 3D morphology of hydrofracturing crack networks result from comprehensive effect of geostress difference and material heterogeneity. A quantitative description of the 3D fracture

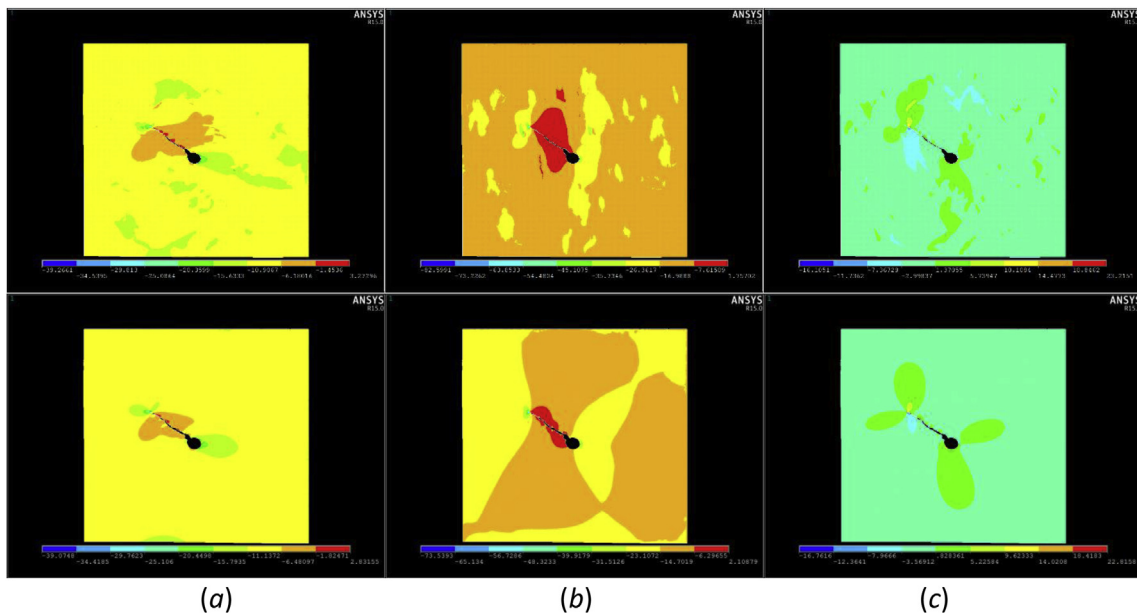


Fig. 9. Simulation results of the stresses in the vicinity of the wellbore of the heterogeneous model (top row) and the homogeneous model (bottom row) subjected to the geostress ratio 1:1.5: (a) X-component stress, (b) Y-component stress, and (c) shear stress in X-Y plane, respectively.

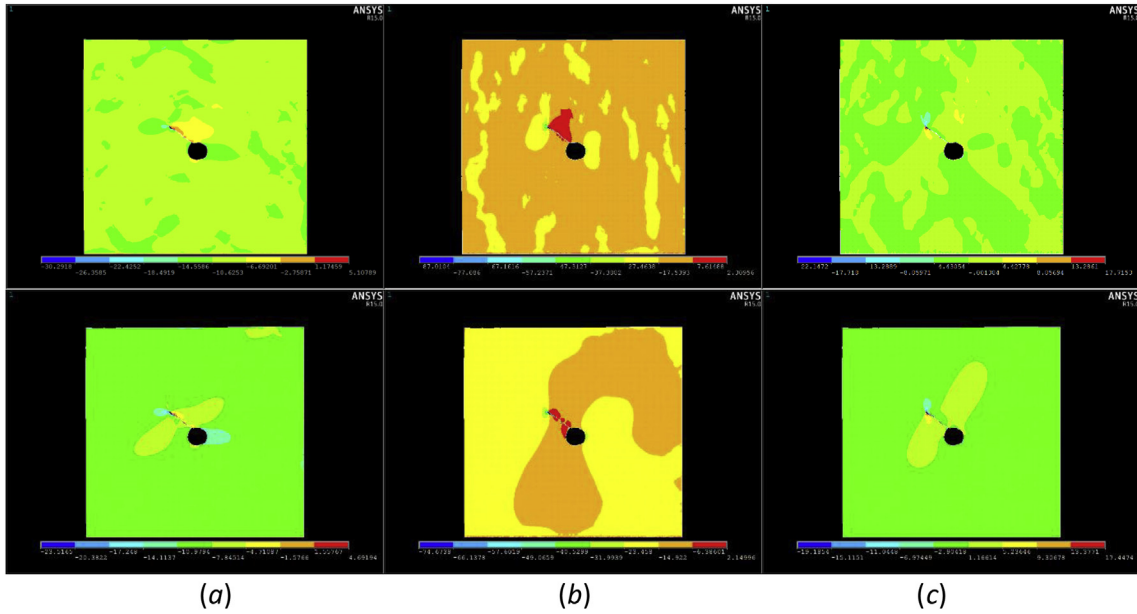


Fig. 10. Simulation results of the stresses in the vicinity of the wellbore of the heterogeneous model (top row) and the homogeneous model (bottom row) subjected to the geostress ratio 1:1.7: (a) X-component stress, (b) Y-component stress, and (c) shear stress in X-Y plane, respectively.

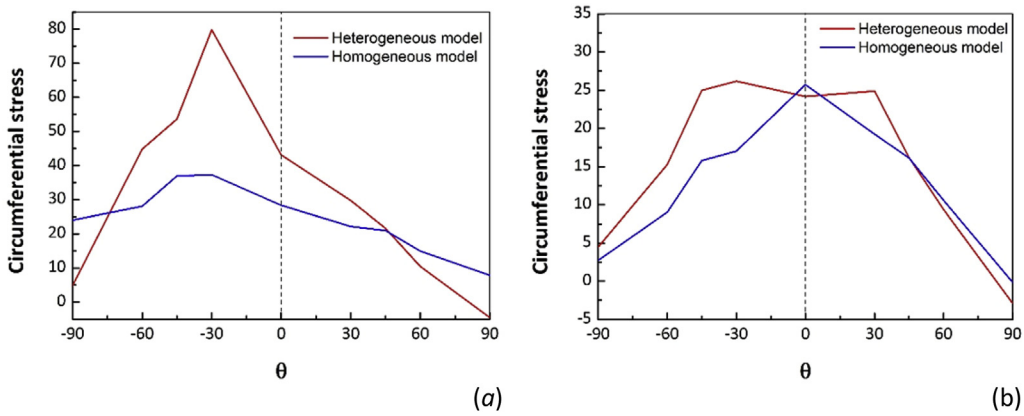


Fig. 11. Calculation results of the circumferential stress along various propagation azimuths under the geostress ratios of 1:1.5 (a) and 1:1.7 (b).

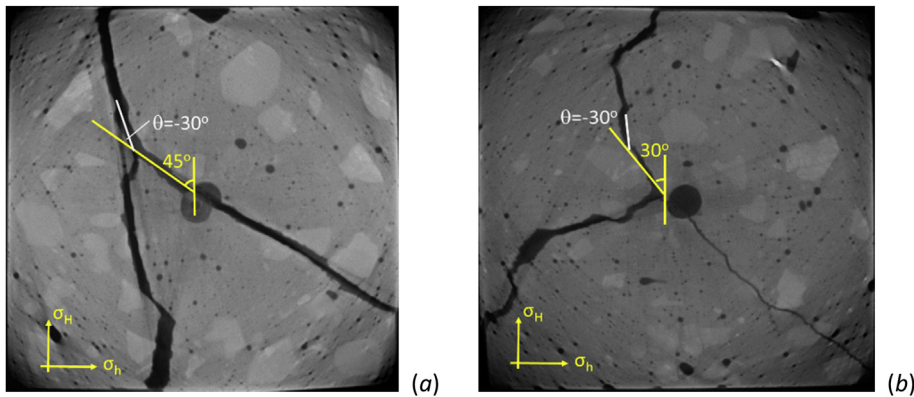


Fig. 12. Experimental observation of the crack propagation azimuths of the heterogeneous specimens under the horizontal geostress ratio 1:1.5 (a) and 1:1.7 (b).

network helps to understand the comprehensive influence of geostress difference and material heterogeneity on hydraulic fracturing of rock. Previous investigations show the fracture network of

rock is characterized by fractal (Chilès, 1988; Falconer, 1990; Sato et al., 1999; Xie, 1993). Similarly, we adopted fractal theory (Gang and Ju, 2008; Xie, 1993; Ju et al., 2014) to characterize and

analyze the 3D morphology of hydrofracturing crack networks of both heterogeneous and homogeneous rock specimens.

It is shown that the fractal dimension quantifies the characteristics of fracture population and distribution (Charkaluk et al., 1998; Gang and Ju, 2008; Sato et al., 1999; Xie, 1993). The higher the degree of growth and development of fractures is, the larger the fractal dimension of the fracture network is. In order to measure the fractal dimension of hydrofracturing cracks in heterogeneous glutenite, the box-counting method (Charkaluk et al., 1998; Gang and Ju, 2008; Sato et al., 1999; Xie, 1993; Ju et al., 2014) was first applied to the 2D transverse CT images of the fractures. Fig. 13 illustrates the binarized 2D CT image of the fractures extracted from a selected 2D cross section of the specimen using the image processing and segmentation methods (Ju et al., 2014). The box-covering method for calculating the fractal dimension of the fracture network is also demonstrated in Fig. 13. According to the box-counting method, the fractal dimension of the 2D fracture network can be expressed as

$$D_B = \lim_{k \rightarrow \infty} \frac{\ln N_{\delta_k}}{-\ln \delta_k}, \quad (6)$$

where D_B refers to the fractal dimension of the fracture network, δ_k is the side length of the k th covering grid, N_{δ_k} is the number of the effective grids that covering the fracture; k means the k th covering.

The calculation procedure is described as follow:

- (1) Converting the original grey CT image of fractures into the binarized image using the binarization and segmentation methods, as shown in Fig. 13. The fractures are represented by black pixels, while the matrix is characterized by white pixels.
- (2) Covering the binarized image of fractures with grids of the side length of δ_k , and counting the covering number N_{δ_k} . Halving the side length subdivides the grids into the smaller

one δ_{k+1} . Continuously repeating this process yields an array of N_{δ_k} corresponding to δ_k . Plotting the covering number N_{δ_k} against δ_k in a double logarithmic coordinates generates the curve of $\ln N_{\delta_k} \sim \ln(1/\delta_k)$, of which the slope of the line represents the fractal dimension D_B .

For the fractal description of the 3D morphology of fracture network, similar box-counting method was applied. The computer software MIMICS[®] was employed to construct the 3D model using the 2D images. A total of 640 2D slices was used to construct a 3D model. Fig. 14 demonstrates the method that was proposed to cover the spatially distributed cracks by consecutively subdividing the voxels into the smaller ones. The relationship between the covering number N_{δ_k} and the box side length δ_k can also be attained. A computer program (Ju et al., 2013) was then developed to determine the fractal dimension of the 3D fracture network based on the data matrix $-\ln N_{\delta_k}, \ln(1/\delta_k)$ using the similar principle for 2D treatment.

4.2. Analysis of the fractal characteristics of hydrofracturing crack networks

The fractal dimensions of the 3D hydrofracturing crack networks of the heterogeneous materials under various geostress ratios were obtained using the aforementioned method. Fig. 15 plots the calculation results of fractal dimensions against horizontal geostress ratios, where the vertical coordinate stands for the calculated fractal dimension of 3D hydrofracturing crack networks (D_B), and the lateral coordinate refers to the ratio of the maximum horizontal geostress component to the minimum horizontal geostress component (σ_H/σ_h). To elucidate the effect of material heterogeneity on hydrofracturing behavior, similar method was applied to acquiring the fractal characteristics of the hydrofracturing networks of homogeneous media. The handling results were also plot in Fig. 15 for the sake of comparison.

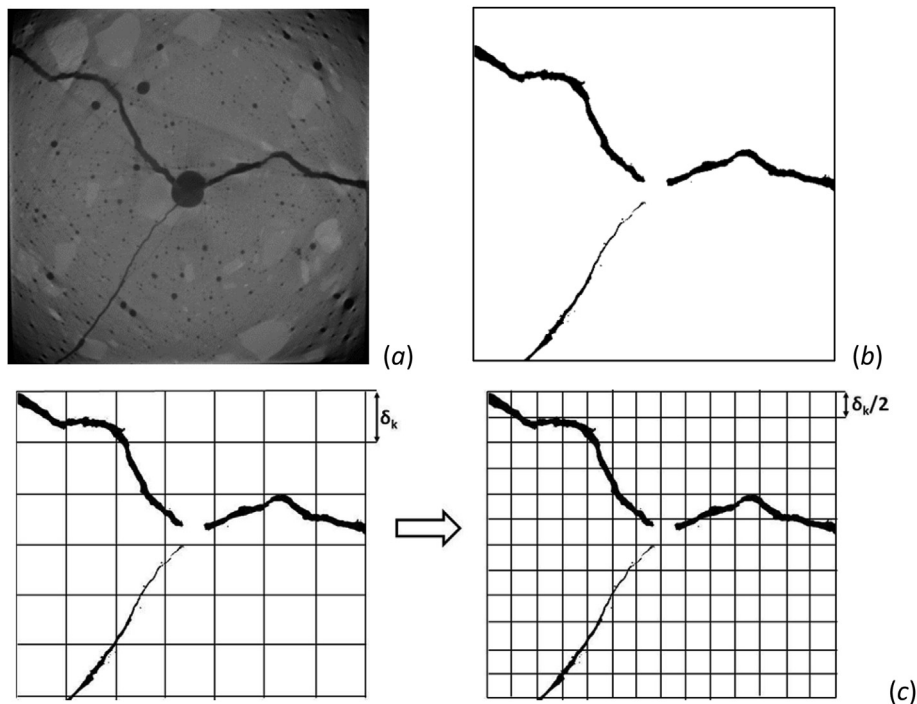


Fig. 13. Illustration of 2D fracture network and box-counting method for determining the fractal dimensions, (a) original grey CT image of fractures, (b) binarized image of fractures, (c) the k th covering with a grid size of δ_k , and (d) the $(k+1)$ th covering with a grid size of δ_{k+1} .

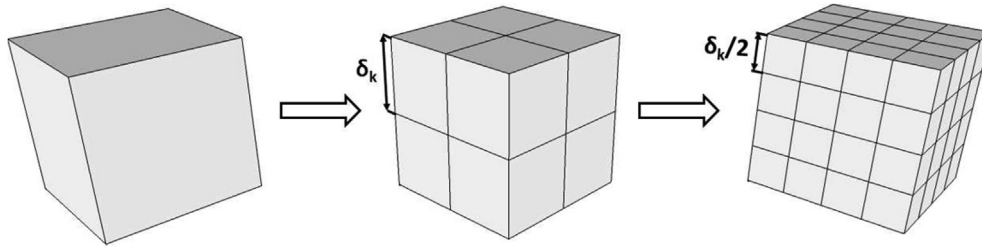


Fig. 14. Illustration of the 3D box-counting method for determining the fractal dimension of 3D morphology of hydrofracturing crack network.

The results indicate that for both heterogeneous and homogeneous rock models there is a watershed in the fractal characteristics of hydrofracturing crack networks, that is, the stress ratio, $\sigma_H/\sigma_h=1.5$, separates the fractal characteristics of hydrofracturing crack networks into two parts. The fractal dimension at the stress ratio of 1.5 reaches the maximum value. It means that once the stress ratio σ_H/σ_h is over 1:1.5, i.e. reaches 1:1.7, the fractal dimension of hydrofracturing crack network quickly decreases with increasing the geostress ratio, which implies that when increasing geostress difference the degree of growth and complexity of hydrofracturing crack network gradually diminishes. The geostress ratio 1:1.7 appears to be the threshold value at which the fracture network that is composed of multiple fractures turns to be a single double-wing fracture. The fractal dimension of the hydrofracturing crack network is negatively related to the degree of geostress difference. It means that the larger the degree of geostress difference is, the smaller the fractal dimension of the crack network is, and then the more likely the single crack occur. Both heterogeneous and homogeneous rock models exhibit the same variation tendency of the fractal characteristics of hydrofracturing crack network. This result reflects the controlling effect of geostress difference on hydraulic fracturing performance of reservoir rocks.

It should be noticed that the fractal dimension at the stress ratio of 1.3 appears to be lower than that at the stress ratio of 1.0, which leads to the distinct variation of fractal characteristics before the watershed stress ratio is reached, that is, the fractal dimension decreases first and then increases after the stress ratio exceeds 1.3. One of the possibilities that cause this inconsistency is attributed to the randomness of crack initiation and propagation due to the scatterness in the properties of cement materials that were used to model rocks. The scatterness in the strengths, including compressive strength, tensile strength, and shear strength, plasticity and even fracture toughness impacts the performance of crack initiation and propagation of models. Particularly, existence of the embedded randomly distributed gravels has intensified the degree of scatterness.

Furthermore, it is noteworthy that comparing the results of the different rock specimens indicates that the fractal dimension of hydrofracturing crack network of a heterogeneous model is larger than that of a homogeneous model. There is a significant difference of D_B value between 1.0 and 1.3 stress ratios for heterogeneous samples compared to that of homogeneous samples. In fact, the fractal dimension of the fracture network D_B that was used to characterize different fracture patterns is a comprehensive index, which reflects not only the distribution nature of fractures but also the tortuosity of fracture surface morphology. The CT images of fractures indicate that the fracture surface at the ratio of 1.0 appears to be more tortuous than that at the ratio of 1.3 for heterogeneous samples. From the authors' points of view, this is attributed to the effects of gravels on fracture initiation and propagation within heterogeneous specimens. On the contrary, Fig. 6 indicates that fracture surfaces of the homogenous samples are quite close to flat planes when the stress ratios are 1.0 and 1.3. This explains why there is a significant difference of D_B between stress ratios 1.0 and 1.3 for heterogeneous specimens comparing with that of homogeneous samples. It means that a heterogeneous model exhibits more tortuous fracture morphology and a more developed crack network than a homogeneous model with the same degree of geostress difference. The fractal dimension D_B positively relates to the degree of heterogeneity of rock media. This verifies the significant effect of material heterogeneity on the hydraulic fracturing performance of reservoir rocks.

5. Conclusions

This study investigates the effects of geostress difference and material heterogeneity on the hydraulic fracturing performance of heterogeneous reservoir glutenite. Advanced experimental techniques, including modeling tests, triaxial hydrofracturing tests, and high-resolution microfocus computed tomography, were employed to probe the effects of geostress difference and material heterogeneity on the characteristics of hydrofracturing cracks, such as

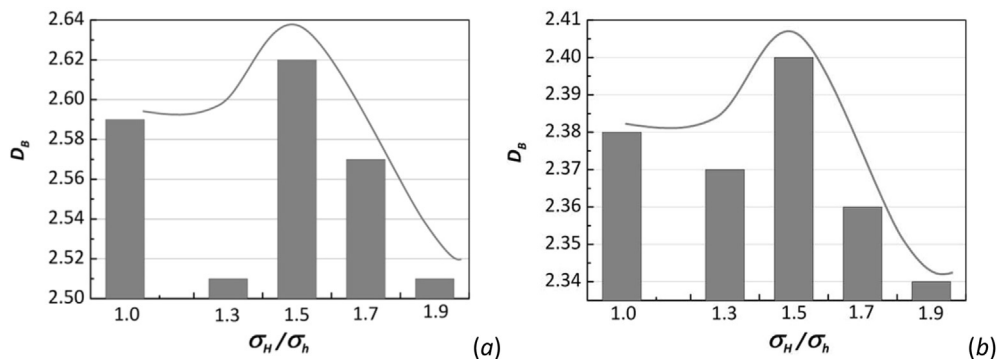


Fig. 15. Fractal dimensions of 3D hydrofracturing crack networks of both heterogeneous models (a) and homogeneous models (b) varying with the applied geostress ratios.

initiation, propagation, growth, and population. Fractal theories were applied to characterizing the 3D hydrofracturing crack networks of both heterogeneous and homogeneous rock samples. The main conclusions are as follow:

- (1) Both horizontal geostress difference and material heterogeneity has significant influence on the characteristics of hydrofracturing cracks in heterogeneous reservoir rock. When the degree of horizontal geostress difference is higher, that is, the geostress ratio reaches 1:1.7, it is more likely to have a double-wing single crack than multiple twist cracks, no matter the tested rock model is heterogeneous or homogeneous. The geostress ratio 1:1.7 appears to be a threshold value at which the multiple hydrofracturing cracks occur in rocks. The horizontal geostress difference is the predominant factor that influences the fracture pattern of reservoir rocks. In contrast, if the degree of horizontal geostress difference is lower, that is, the geostress ratio is below 1:1.7, multiple twist cracks rather than a single crack occurs. In the context of this sort, the distributed gravels remarkably influence the initiation and propagation of hydrofracturing cracks, which implies that material heterogeneity plays the predominant role in affecting the crack initiation and propagation performance.
- (2) The analysis of the stress states in the neighborhoods of the wellbore and the initial crack using fracture mechanics theory and finite element methods quantitatively elucidates the mechanisms through which horizontal geostress difference and material heterogeneity induce and control the hydrofracturing crack initiation and propagation. The analytical results are in good agreement with the experimental measurement.
- (3) The fractal characterization of the 3D hydrofracturing crack network of rock models verifies the distinct contribution of geostress difference and material heterogeneity to controlling the crack initiation and propagation in heterogeneous reservoir rock. The fractal analysis results are consistent with the analysis of fracture patterns of the tested rock models. It is shown that the fractal dimension of the crack network is a comprehensive measure of the coupled effects of geostress difference and material heterogeneity on the hydrofracturing performance of reservoir rock. The fractal dimension of the hydrofracturing crack network is positively related to the degree of material heterogeneity and negatively related to the degree of geostress difference.

Acknowledgements

The authors gratefully acknowledge the financial support of the National Natural Science Foundation of China (Grant 51374213), National Natural Science Fund for Distinguished Young Scholars of China (Grant 51125017), Fund for Innovative Research and Development Group Program of Jiangsu Province (Grant 2014-27), Science Fund for Creative Research Groups of the National Natural Science Foundation of China (Grant 51421003), and the Priority Academic Program Development of Jiangsu Higher Education Institutions (Grant PAPD2014). The authors would also like to express their gratitude to the editors and the anonymous reviewers for their valuable comments and suggestions, which have greatly improved this paper.

References

Adriaensens, P., Storme, L., Carleer, R., Vanderzande, D., Gelan, J., Litvinov, V.M., Marissenf, R., 2000. Visualization of tensile stress induced material response at

- a crack tip in polymers under critical load by NMR imaging. *Macromolecules* 33 (13), 4836–4841.
- Advani, S.H., Lee, J., 1982. Finite element model simulations associated with hydraulic fracturing. *Soc. Pet. Eng. J.* 22 (2), 209–218.
- Al-Busaidi, A., Hazzard, J., Young, R., 2005. Distinct element modeling of hydraulically fractured Lac du Bonnet granite. *J. Geophys. Res. Solid Earth* 110 (110), 351–352 (1978–2012).
- Alpern, J., Marone, C., Elsworth, D., Belmonte, A., Connelly, P., 2012. Exploring the physicochemical processes that govern hydraulic fracture through laboratory experiments. In: 46th US Rock Mechanics/Geomechanics Symposium. American Rock Mechanics Association. ARMA 2678.
- Beugelsdijk, L.J.L., De Pater, C.J., Sato, K., 2000. Experimental hydraulic fracture propagation in a multi-fractured medium. In: SPE Asia Pacific Conference on Integrated Modelling for Asset Management. Society of Petroleum Engineers. SPE 59419.
- Bunger, A.P., Kear, J., Dyskin, A.V., Pasternak, E., 2015. Sustained acoustic emissions following tensile crack propagation in a crystalline rock. *Int. J. Fract.* 193 (1), 87–98.
- Castano, A.F., Sondergeld, C.H., Rai, C.S., 2010. Estimation of uncertainty in microseismic event location associated with hydraulic fracturing. In: Tight Gas Completions Conference. Society of Petroleum Engineers. SPE 135325.
- Charkaluk, E., Bigerelle, M., Iost, A., 1998. Fractals and fracture. *Eng. Fract. Mech.* 61 (1), 119–139.
- Chen, L.H., Chen, W.C., Chen, Y.C., Benyamin, L., Li, A.J., 2014. Investigation of hydraulic fracture propagation using a post-peak control system coupled with acoustic emission. *Rock Mech. Rock Eng.* 48 (3), 1233–1248.
- Chen, Y., Nagaya, Y., Ishida, T., 2015. Observations of fractures induced by hydraulic fracturing in anisotropic granite. *Rock Mech. Rock Eng.* 48 (4), 1455–1461.
- Chilès, J.P., 1988. Fractal and geostatistical methods for modeling of a fracture network. *Math. Geol.* 20 (6), 631–654.
- Chitralla, Y., Moreno, C., Sondergeld, C., Rai, C., 2013. An experimental investigation into hydraulic fracture propagation under different applied stresses in tight sands using acoustic emissions. *J. Pet. Sci. Eng.* 108 (3), 151–161.
- Cipolla, C., Maxwell, S., Mack, M., Downie, R., 2012a. A practical guide to interpreting microseismic measurements. In: North American Unconventional Gas Conference and Exhibition. Society of Petroleum Engineers. SPE 144067.
- Cipolla, C., Weng, X., Mack, M., Ganguly, U., Gu, H., Kresse, O., Cohen, C., 2012b. Integrating microseismic mapping and complex fracture modeling to characterize fracture complexity. In: SPE Hydraulic Fracturing Technology Conference. Society of Petroleum Engineers. SPE140185.
- Detournay, C., Cundall, P.A., Damjanac, B., 2013. Hydraulic fracture simulation: comparison with exact solutions. *Res. Appl. Struct. Eng. Mech. Comput.* 603–608.
- Dong, C.Y., De Pater, C.J., 2001. Numerical implementation of displacement discontinuity method and its application in hydraulic fracturing. *Comput. Method. Appl. Mech. Eng.* 191 (8–10), 745–760.
- Dong, C.Y., De Pater, C.J., 2002. Numerical modeling of crack reorientation and link-up. *Adv. Eng. Softw.* 33 (s 7–10), 577–587.
- Espina, C., Baldassa, D., Sorenson, F., Lopez, E., Bonapace, J., Quintavalla, C., 2009. Hydraulic fracturing: modeling and optimization using latest generation logs and conductivity optimization technologies. In: SPE Hydraulic Fracturing Technology Conference. Society of Petroleum Engineers, pp. 493–514.
- Falconer, K.J., 1990. Fractal geometry: mathematical foundation and application. *Biometrics* 46 (4), 499.
- Fjær, E., Holt, R.M., Horsrud, P., Raaen, A.M., Risnes, R., 2008. Stresses around boreholes. Borehole failure criteria. In: Fjær, E., Holt, R.M. (Eds.), *Petroleum Related Rock Mechanics*, second ed. Elsevier, Amsterdam, pp. 135–174.
- Gang, W., Ju, T., 2008. Study of minimum box-counting method for image fractal dimension estimation. In: International Conference on Electricity Distribution. IEEE Comput. Soc. 1–5.
- Garcia, J.G., Teufel, L.W., 2005. Numerical simulation of fully coupled fluid-flow/geomechanical deformation in hydraulically fractured reservoirs. In: SPE Production Operations Symposium. Society of Petroleum Engineers. SPE 94062.
- Geertsma, J., De Klerk, F., 1969. A Rapid method of predicting width and extent of hydraulically induced fractures. *J. Pet. Technol.* 21 (12), 1571–1581.
- Gesret, A., Noble, M., Desassis, N., Romary, T., 2013. Microseismic monitoring-consequences of velocity model uncertainties on event location uncertainties. In: 75th EAGE Conference & Exhibition Incorporating SPE EUROPEC 2013. European Association of Geoscientists and Engineers. SPE 178548.
- Gomaa, A.M., Zhang, B., Chen, J., Qu, Q., Nelson, S., 2014. Using NMR technology to study the flow of fracture fluid inside shale formation. In: SPE International Symposium and Exhibition on Formation Damage Control. Society of Petroleum Engineers, pp. 667–680.
- Grayson, S., Kamerling, M., Pirie, I., Swager, L., 2015. NMR-enhanced natural fracture evaluation in the monterey shale. In: SPWLA 56th Annual Logging Symposium. Society of Petrophysicists and Well-log Analysts. SPWLA 2015.
- Gu, H., Siebrits, E., 2008. Effect of formation modulus contrast on hydraulic fracture height containment. In: SPE Production & Operations. Society of Petroleum Engineers. SPE 103822.
- Gu, H., Siebrits, E., Sabourov, A., 2008. Hydraulic fracture modeling with bedding plane interfacial slip. In: SPE Eastern Regional/AAPG Eastern Section Joint Meeting. Society of Petroleum Engineers. SPE 117445.
- Guo, T., Zhang, S., Qu, Z., Zhou, T., Xiao, Y., Gao, J., 2014. Experimental study of hydraulic fracturing for shale by stimulated reservoir volume. *Fuel* 128 (14), 373–380.

- Gutierrez Murillo, G., Sanchez, A.C., Rios, A., Arguello, L., 2010. Microseismic hydraulic fracture monitoring to determine the fracture geometry in Coyotes field, Chicontepec. In: SPE Latin American and Caribbean Petroleum Engineering Conference. Society of Petroleum Engineers. SPE 139155.
- Hampton, J.C., Hu, D., Matzar, L., Gutierrez, M., 2014. Cumulative volumetric deformation of a hydraulic fracture using acoustic emission and micro-CT imaging. In: 48th US Rock Mechanics/Geomechanics Symposium. American Rock Mechanics Association. ARMA 7041.
- Hiyama, M., Shimizu, H., Ito, T., Tamagawa, T., Tezuka, K., 2013. Distinct element analysis for hydraulic fracturing in shale—Effect of brittleness on the fracture propagation. In: 47th U.S. Rock Mechanics/Geomechanics Symposium. American Rock Mechanics Association. ARMA 659.
- Hossain, M.M., Rahman, M., 2008. Numerical simulation of complex fracture growth during tight reservoir stimulation by hydraulic fracturing. *J. Pet. Sci. Eng.* 60 (2), 86–104.
- Inui, S., Ishida, T., Nagaya, Y., Nara, Y., Chen, Y., Chen, Q., 2014. AE monitoring of hydraulic fracturing experiments in granite blocks using supercritical CO₂, water and viscous oil. In: 48th US Rock Mechanics/Geomechanics Symposium. American Rock Mechanics Association, pp. 31–36.
- Jeffrey, R.G., Bungler, A., Lecampion, B., Zhang, X., Chen, Z.R., van As, A., Allison, D.P., De Beer, W., Dudley, J.W., Siebrits, E., 2009. Measuring hydraulic fracture growth in naturally fractured rock. In: SPE Annual Technical Conference and Exhibition. Society of Petroleum Engineers. SPE124919.
- Johnston, R., Shallow, J., 2011. Ambiguity in microseismic monitoring. In: SEG Annual Meeting. Society of Exploration Geophysicists. SEG 1514.
- Ju, Y., Liu, H.B., Liu, J.H., Tian, K.P., Song, W., Song, H., 2011. Investigation on thermophysical properties of reactive powder concrete. *Sci. China Technol. Sci.* 54, 3382–3403.
- Ju, Y., Liu, H.B., Sheng, G.H., Wang, H.J., 2010. Experimental study of dynamic mechanical properties of reactive powder concrete under high-strain-rate impacts. *Sci. China Technol. Sci.* 53, 2435–2449.
- Ju, Y., Jia, Y.D., Liu, H.B., Chen, J., 2007. Mesomechanism of steel fiber reinforcement and toughening of reactive powder concrete. *Sci. China Technol. Sci.* 50 (6), 815–832.
- Ju, Y., Wang, L., Liu, H., Tian, K., 2015. An experimental investigation of the thermal spalling of polypropylene-fibered reactive powder concrete exposed to elevated temperatures. *Sci. Bull.* 60, 1–19.
- Ju, Y., Xing, M.X., Sun, H.F., 2013. Computer Program for Extracting and Analyzing Fractures in Rocks and Concretes. Software Copyright Registration #0530646, Beijing (in Chinese).
- Ju, Y., Yang, Y.M., Chen, J.L., Liu, P., Dai, T., Guo, Y.C., Zheng, L.G., 2016. 3D reconstruction of low-permeability heterogeneous glutenites and numerical simulation of hydraulic fracturing behavior (in Chinese). *Chin. Sci. Bull.* 61, 82–93.
- Ju, Y., Zheng, J., Epstein, M., Sudak, L., Wang, J., Zhao, X., 2014. 3D numerical reconstruction of well-connected porous structure of rock using fractal algorithms. *Comput. Method. Appl. Mech. Eng.* 279 (9), 212–226.
- Kaestner, A., Lehmann, E., Stamparoni, M., 2008. Imaging and image processing in porous media research. *Adv. Water Resour.* 31 (9), 1174–1187.
- Koceir, M., Tiab, D., 2000. Influence of stress and lithology on hydraulic fracturing in Hassi Messaoud reservoir, Algeria. In: SPE/AAPG Western Regional Meeting. Society of Petroleum Engineers. SPE 62608.
- Kresse, O., Cohen, C., Weng, X., Wu, R., Gu, H., 2011. Numerical modeling of hydraulic fracturing in naturally fractured formations. In: 45th US Rock Mechanics/Geomechanics Symposium. Society of Petroleum Engineers. American Rock Mechanics Association. ARMA 363.
- Kresse, O., Weng, X., Gu, H., Wu, R., 2013. Numerical modeling of hydraulic fractures interaction in complex naturally fractured formations. *Rock Mech. Rock Eng.* 46 (3), 555–568.
- Li, L., Meng, Q., Wang, S., Li, G., Tang, C., 2013. A numerical investigation of the hydraulic fracturing behaviour of conglomerate in Glutenite formation. *Acta Geotech.* 8 (6), 597–618.
- Li, Q., Xing, H., Liu, J., Liu, X., 2015. A review on hydraulic fracturing of unconventional reservoir. *Petroleum* 1 (1), 8–15.
- Liu, H., Wang, H., Wu, H., Wang, X., 2014a. A proppant settling model and its application to the hydraulic fracturing process. *Oil Gas-Eur. Mag.* 40 (2), 109–112.
- Liu, J., Feng, X., Fei, G., 2003. Study on mathematical model of three dimensional hydraulic fracturing. *Chin. J. Rock Mech. Eng.* 22 (12), 2042–2046.
- Liu, P., Ju, Y., Zhang, Q.G., Ranjith, P.G., Zhang, Q.B., Zhao, X., 2016. CT identification of 3D propagation and distribution of hydrofracturing cracks of low-permeability reservoir Rocks. *Rock Mech. Rock Eng.* (Under Review).
- Liu, Z., Chen, M., Zhang, G., 2014b. Analysis of the influence of a natural fracture network on hydraulic fracture propagation in Carbonate Formations. *Rock Mech. Rock Eng.* 47 (2), 575–587.
- Mahrer, K.D., 1999. A review and perspective on far-field hydraulic fracture geometry studies. *J. Pet. Sci. Eng.* 24 (1), 13–28.
- Maxwell, S., 2009. Microseismic location uncertainty. *CSEG Rec.* 34 (4), 41–46.
- Maxwell, S., Bennett, L., Jones, M., Walsh, J., 2010. Anisotropic velocity modeling for microseismic processing: part 1—impact of velocity model uncertainty. In: SEG Annual Meeting. Society of Exploration Geophysicists. SEG 2130.
- Maxwell, S.C., Cipolla, C.L., 2011. What does microseismicity tell us about hydraulic fracturing?. In: SPE Annual Technical Conference and Exhibition. Society of Petroleum Engineers. SPE 146932.
- Nabipour, A., 2013. Experimental and Numerical Study of Ultrasonic Monitoring of Hydraulic Fracture Propagation. Curtin University. Doctoral thesis.
- Nasehi, M.J., Mortazavi, A., 2013. Effects of in-situ stress regime and intact rock strength parameters on the hydraulic fracturing. *J. Pet. Sci. Eng.* 108 (4), 211–221.
- Nassir, M.J., Settari, A., Wan, R., 2010. Modeling shear dominated hydraulic fracturing as a coupled fluid–solid interaction. In: International Oil and Gas Conference and Exhibition. Society of Petroleum Engineers, pp. 8–10.
- Nordgren, R., 1972. Propagation of a vertical hydraulic fracture. *Soc. Pet. Eng. J.* 12 (4), 306–314.
- Peng, S., Zhang, J., 2007. *Engineering Geology for Underground Rocks*. Springer, Berlin.
- Potyondy, D., Cundall, P., 2004. A bonded-particle model for rock. *Int. J. Rock Mech. Min.* 41 (8), 1329–1364.
- Renard, F., Bernard, D., Desrues, J., Ougier-Simonin, A., 2009. 3D imaging of fracture propagation using synchrotron X-ray microtomography. *Earth Planet. Sci. Lett.* 286 (s 1–2), 285–291.
- Richard, P., Cheyrezy, M., 1994. Reactive powder concretes with high ductility and 200–800 MPa compressive strength. *ACISP* 114, 507–518.
- Richard, P., Cheyrezy, M., 1995. Composition of reactive powder concretes. *Cem. Concr. Res.* 25 (7), 1501–1511.
- Rungamornrat, J., Wheeler, M.F., Mear, M.E., 2005. A numerical technique for simulating nonplanar evolution of hydraulic fractures. In: SPE Annual Technical Conference and Exhibition. SPE 96968.
- Sarmadivaleh, M., Rasouli, V., 2015. Test design and sample preparation procedure for experimental investigation of hydraulic fracturing interaction modes. *Rock Mech. Rock Eng.* 48 (1), 93–105.
- Sato, K., Hashida, T., Takahashi, H., Takahashi, T., Hayashi, K., 1999. Relationship between fractal dimension of multiple microcracks and fracture energy in rocks. *Geotherm. Sci. Technol.* 6 (1–4), 1–23.
- Settari, A., Cleary, M., 1982. Development and testing of a pseudo-three-dimensional model of hydraulic fracture geometry. *SPE Product. Eng.* 1 (6), 449–466.
- Shen, G., Wu, Z., Zhang, J., 2015. *Advances in Acoustic Emission Technology: Proceedings of the World Conference on Acoustic Emission-2013*, 2015th ed. Springer, Shanghai.
- Shimizu, H., Hiyama, M., Ito, T., Tamagawa, T., Tezuka, K., 2014. Flow-coupled DEM simulation for hydraulic fracturing in pre-fractured rock. In: 48th US Rock Mechanics/Geomechanics Symposium. American Rock Mechanics Association. ARMA 7365.
- Shimizu, H., Murata, S., Ishida, T., 2011. The distinct element analysis for hydraulic fracturing in hard rock considering fluid viscosity and particle size distribution. *Int. J. Rock Mech. Min.* 48 (5), 712–727.
- Sih, G.C., Madenci, E., 1983. Crack growth resistance characterized by the strain energy density function. *Eng. Fract. Mech.* 18 (18), 1159–1171.
- Simonson, E.R., Abou-Sayed, A.S., Clifton, R.J., 1978. Containment of massive hydraulic fractures. *Soc. Pet. Eng. J.* 18 (1), 27–32.
- Stanchits, S., Surdi, A., Gathogo, P., Edelman, E., Suarez-Rivera, R., 2014. Onset of hydraulic fracture initiation monitored by acoustic emission and volumetric deformation measurements. *Rock Mech. Rock Eng.* 47 (5), 1521–1532.
- Taleghani, A.D., 2010. Fracture re-initiation as a possible branching mechanism during hydraulic fracturing. In: 44th US Rock Mechanics Symposium and 5th U.S.–Canada Rock Mechanics Symposium. American Rock Mechanics Association. ARMA 278.
- Tang, C., Tham, L., Lee, P., Yang, T., Li, L., 2002. Coupled analysis of flow, stress and damage (FSD) in rock failure. *Int. J. Rock Mech. Min.* 39 (4), 477–489.
- Teufel, L.W., Clark, J.A., 1984. Hydraulic fracture propagation in layered rock: experimental studies of fracture containment. *Soc. Pet. Eng. J.* 24 (1), 19–32.
- Thiercelin, M., Ben-Naceur, K., Lemanczyk, Z., 1985. Simulation of three-dimensional propagation of a vertical hydraulic fracture. In: SPE/DOE Low Permeability Gas Reservoirs Symposium. Society of Petroleum Engineers. SPE 13861.
- van der Baan, M., Eaton, D., Dusseault, M., 2013. Microseismic monitoring developments in hydraulic fracture stimulation. In: Bungler, A.P., McLennan, J., Jeffrey, R. (Eds.), *Effective and Sustainable Hydraulic*. Intech, Australia, pp. 339–466.
- Vandamme, L., Curran, J.H., 1989. A three-dimensional hydraulic fracturing simulator. *Int. J. Numer. Meth. Eng.* 28 (4), 909–927.
- Wang, H., Liu, H., Wu, H., Zhang, G., Wang, X., 2012. A 3D nonlinear fluid–solid coupling model of hydraulic fracturing for multilayered reservoirs. *Pet. Sci. Technol.* 30 (21), 2273–2283.
- Wang, K., Zhang, Q., Xia, X., Wang, L., Liu, X., 2015. Analysis of hydraulic fracturing in concrete dam considering fluid–structure interaction using XFEM-FVM model. *Eng. Fail. Anal.* 57, 399–412.
- Wang, S., Sloan, S., Fityus, S., Griffiths, D., Tang, C., 2013. Numerical modeling of pore pressure influence on fracture evolution in brittle heterogeneous rocks. *Rock Mech. Rock Eng.* 46 (5), 1165–1182.
- Warpinski, N., Teufel, L., 1987. Influence of geologic discontinuities on hydraulic fracture propagation (includes associated papers 17011 and 17074). *J. Pet. Technol.* 39 (2), 209–220.
- Warpinski, N.R., Mayerhofer, M.J., Vincent, M.C., Cipolla, C.L., Lonon, E., 2009. Stimulating unconventional reservoirs: maximizing network growth while optimizing fracture conductivity. *J. Can. Pet. Technol.* 48 (10), 39–51.
- Warpinski, N.R., Waltman, C.K., Weijers, L., 2010. An evaluation of microseismic monitoring of lenticular tight-sandstone stimulations. *SPE Prod. Oper.* 25 (4), 498–508.
- Wasantha, P., Ranjith, P., Zhang, Q., Xu, T., 2015. Do joint geometrical properties

- influence the fracturing behaviour of jointed rock? An investigation through joint orientation. *Geomech. Geophys. Geo. Energy Geo. Resour.* 1 (1–2), 3–14.
- Waters, G.A., Dean, B.K., Downie, R.C., Kerrihard, K.J., Austbo, L., McPherson, B., 2009. Simultaneous hydraulic fracturing of adjacent horizontal wells in the woodford shale. In: *SPE Hydraulic Fracturing Technology Conference*. Society of Petroleum Engineers. SPE 119635.
- Wu, H., Golovin, E., Shulkin, Y., Chudnovsky, A., Dudley, J., Wong, G., 2008a. Observations of hydraulic fracture initiation and propagation in a brittle polymer. In: *42nd U.S. Rock Mechanics Symposium*. American Rock Mechanics Association. ARMA 321.
- Wu, R., Bunger, A., Jeffrey, R., Siebrits, E., 2008b. A comparison of numerical and experimental results of hydraulic fracture growth into a zone of lower confining stress. In: *42nd US Rock Mechanics Symposium*. American Rock Mechanics Association. ARMA 267.
- Xie, H., 1993. *Fractals in Rock Mechanics*. A. A. Balkema, Netherlands.
- Xie, H.P., Gao, F., Ju, Y., Xie, L.Z., Yang, Y.M., Wang, J., 2016. Novel idea of the theory and application of 3D volume fracturing for stimulation of shale gas reservoirs. *Chin. Sci. Bull.* 61, 36–46 (In Chinese).
- Yang, T., Tham, L., Tang, C., Liang, Z., Tsui, Y., 2004. Influence of heterogeneity of mechanical properties on hydraulic fracturing in permeable rocks. *Rock Mech. Rock Eng.* 37 (4), 251–275.
- Zhang, C.Q., Feng, X.T., Zhou, H., Zhang, C.S., Wu, S.Y., 2010. Estimation of in-situ stress state at the maximum depth of the Jinping tunnels, China. In: *5th International Symposium on In-situ Rock Stress*, pp. 345–350. ISRSV 2010, August 25–27, Beijing, China.
- Zhang, G.M., Liu, H., Zhang, J., Wu, H.A., Wang, X.X., 2011. Three-dimensional finite element numerical simulation of horizontal well hydraulic fracturing. *Eng. Mech.* 28 (2), 101–106.
- Zhang, G.Q., Fan, T., 2014. A high-stress tri-axial cell with pore pressure for measuring rock properties and simulating hydraulic fracturing. *Measurement* 49 (3), 236–245.
- Zhang, J., Biao, F., Zhang, S., Wang, X., 2014. A numerical study on interference between different layers for a layer-by-layer hydraulic fracture procedure. *Pet. Sci. Technol.* 32 (2), 1512–1519.
- Zhang, X., Jeffrey, R.G., Thiercelin, M., 2007. Deflection and propagation of fluid-driven fractures at frictional bedding interfaces: a numerical investigation. *J. Struct. Geol.* 29 (3), 396–410.
- Zhao, D., Chen, Z., Cai, X., Shuangyang, L.I., 2007. Analysis of distribution rule of geostress in China. *Chin. J. Rock Mech. Eng.* 26, 1265–1271.
- Zhao, H., Chen, M., 2010. Extending behavior of hydraulic fracture when reaching formation interface. *J. Pet. Sci. Eng.* 74 (1), 26–30.
- Zhong, R.Z., Bao, J.Q., Fathi, E., 2014. Fully coupled finite element model to study fault reactivation during multiple hydraulic fracturing in heterogeneous tight formations. In: *SPE Eastern Regional Meeting*. Society of Petroleum Engineers. SPE 171035.
- Zhou, D.S., Zheng, P., He, P., Peng, J., 2016. Hydraulic fracture propagation direction during volume fracturing in unconventional reservoirs. *J. Pet. Sci. Eng.* 141, 82–89.
- Zou, Y.S., Zhang, S.C., Zhou, T., Zhou, X., Guo, T.K., 2016. Experimental investigation into hydraulic fracture network propagation in gas shales using CT scanning technology. *Rock Mech. Rock Eng.* 49 (1), 33–45.